



University of
Massachusetts
Amherst

A Survey Of 557 Ghz Water Vapor Emission In The Ngc 1333 Molecular Cloud

Item Type	Article
Authors	Bergin, EA;Kaufman, MJ;Melnick, GJ;Snell, Ronald L.;Howe, JE
DOI	10.1086/344674
Download date	2026-03-10 16:32:25
Link to Item	https://hdl.handle.net/20.500.14394/3282

accepted by The Astrophysical Journal

A Survey of 557 GHz Water Vapor Emission in the NGC 1333 Molecular Cloud

Edwin A. Bergin

Harvard-Smithsonian Center for Astrophysics, 60 Garden Street, Cambridge, MA 02138

`ebergin@cfa.harvard.edu`

Michael J. Kaufman

*Department of Physics, San Jose State University, One Washington Square, San José, CA
95192-0106*

NASA/Ames Research Center, MS 245-3, Moffett Field, CA 94035

`kaufman@ism.arc.nasa.gov`

Gary J. Melnick

Harvard-Smithsonian Center for Astrophysics, 60 Garden Street, Cambridge, MA 02138

`gmelnick@cfa.harvard.edu`

Ronald L. Snell

Department of Astronomy, University of Massachusetts, Amherst, MA 01003

`snell@astro.umass.edu`

John E. Howe

Department of Astronomy, University of Massachusetts, Amherst, MA 01003

`jhowe@astro.umass.edu`

ABSTRACT

Using NASA's Submillimeter Wave Astronomy Satellite (SWAS) we have examined the production of water in quiescent and shocked molecular gas through a survey of the 556.936 GHz $1_{10} - 1_{01}$ transition of ortho- H_2O in the NGC 1333

molecular core. These observations reveal broad emission lines associated with the IRAS 2, IRAS 4, IRAS 7, and HH7-11 outflows. Towards 3 positions we detect narrow ($\Delta v \sim 2\text{--}3 \text{ km s}^{-1}$) emission lines clearly associated with the ambient gas. The SWAS observations, with a resolution of $\sim 4'$, are supplemented with observations from the Infrared Space Observatory (ISO) and by an unbiased survey of a $\sim 17' \times 15'$ area, with $\sim 50''$ resolution, in the low-J transitions of CO, ^{13}CO , C^{18}O , N_2H^+ , CH_3OH , and SiO.

Using these combined data sets, with consistent assumptions, we find beam-averaged ortho- H_2O abundances of $> 10^{-6}$ relative to H_2 for all four outflows. A comparison of SWAS and ISO water data is consistent with non-dissociative shock models, provided the majority of the ortho- H_2O $1_{10} - 1_{01}$ emission arises from cool post-shock material with enhanced abundances. In the ambient gas the ortho- H_2O abundance is found to lie between $0.1 - 1 \times 10^{-7}$ relative to H_2 and is enhanced when compared to cold pre-stellar molecular cores. A comparison of the water emission with tracers of dense condensations and shock chemistry finds no clear correlation. However, the water emission appears to be associated with the presence of luminous external heating sources which power the reflection nebula and the photodissociation (PDR) region. Simple PDR models are capable of reproducing the water and high-J ^{13}CO emission, suggesting that a PDR may account for the excitation of water in low density undepleted gas as suggested by Spaans & van Dishoeck (2001).

Subject headings: ISM: individual (NGC 1333) – ISM: jets and outflows – ISM: molecules – stars: formation

1. Introduction

Water in cold quiescent molecular gas is theorized to form through a series of ion-molecule chemical reactions that occur early in the reaction sequence that links atomic oxygen to H_2 , the most abundant molecule. Recently NASA's Submillimeter-Wave Astronomy Satellite detected water vapor emission arising from ortho- H_2O (o- H_2O) ground state transition ($1_{10} - 1_{01}$) in numerous dense cores within extended molecular clouds (Snell et al. 2000a). Interestingly, there appears to be a dichotomy in the presence of water detected by SWAS in the sense that emission from water vapor has yet to be detected in cold ($T \leq 15 - 20 \text{ K}$) star-less objects such as TMC-1, B68, or ρ Oph D (Snell et al. 2000a; Bergin & Snell 2002). However, in warmer ($T > 20 \text{ K}$) giant molecular cloud cores, which are associated with sites of multiple star formation, water is readily detected. In each case the

derived water abundance, or abundance limit, is well below theoretical predictions, which is believed to be the result of the freeze-out, or depletion, of oxygen onto grain surfaces (Bergin et al. 2000; Viti et al. 2001; Charnley, Rodgers, & Ehrenfreund 2001). It is not clear if the non-detections in colder cores are the result of any intrinsic difference in the chemistry due to lower temperature, because the excitation conditions for the $1_{10} - 1_{01}$ transition favors emission in warm gas. An alternative has been proposed by Spaans & van Dishoeck (2001) who suggest that the enhanced penetration of ultraviolet (UV) photons in clumpy giant molecular clouds lowers the water vapor column density through photodissociation but enhances the emissivity due to the heating of the gas by the UV radiation. This would allow ion-molecule chemistry to account for water detections in warm giant molecular clouds but colder clouds, such as the star-less objects, require freeze-out of oxygen in the form of H_2O (Spaans & van Dishoeck 2001).

Conditions in the interstellar medium also favor water production through a variety of other mechanisms besides ion-molecule chemistry. Water is believed to be produced efficiently through reactions on the surfaces of cold dust grains (Tielens & Hagen 1982). However, the sublimation temperature of water ice is ~ 110 K (Fraser, Collings, McCoustra, & Williams 2001), much greater than typical dust grain temperatures, so this frozen reservoir is not returned to the gas phase. An additional formation channel is linked to a series of neutral-neutral reactions with activation barriers that can be overcome in gas that is heated to temperatures greater than ~ 300 K (Wagner & Graff 1987; Graff & Dalgarno 1987). Such high temperatures can be found in shocked gas, where material entrained in the bipolar outflows associated with the birth of a star impact the surrounding gas, or in the immediate vicinity of embedded sources. Indeed ESA’s *Infrared Space Observatory* (ISO) and SWAS have convincingly detected water vapor emission in hot gas towards several star-forming regions (Liseau et al. 1996; Ceccarelli et al. 1999; Harwit, Neufeld, Melnick, & Kaufman 1998; Melnick et al. 2000a; Neufeld et al. 2000a; Molinari et al. 2000; Wright et al. 2000; Giannini, Nisini, & Lorenzetti 2001; Maret et al. 2002; Benedettini et al. 2002). The water abundance determined for these regions is also significantly enhanced, by several orders of magnitude, over that estimated in the ambient gas within other nearby clouds by Snell et al. (2000a). These abundance enhancements are expected to persist for $\sim 10^5$ yr, whereupon the molecules deplete onto grain mantles (Bergin, Melnick, & Neufeld 1998). This led to the suggestion by Bergin, Melnick, & Neufeld (1998) that molecular gas could be chemically enriched in H_2O due to repeated exposure to numerous shocks. Furthermore, once the dynamical effects of a shock have dissipated, enhanced abundances of water vapor, above that produced by ion-molecule reactions, might be found as a shock “legacy” in the low velocity quiescent gas.

To examine the production of water in the interstellar medium we present the results

of a biased survey of the NGC 1333 molecular core for emission in the 557 GHz ground state of ortho-H₂O. This source is relatively close, at a distance of 220 pc (Cernis 1990), and is an excellent laboratory to investigate the various potential mechanisms for water formation and emission. First, NGC 1333 is a well known reflection nebula illuminated by two nearby B stars, BD +30.549 (B8V) and SVS 3 (B6V). The radiation from these external sources allows for a search for water emission associated with photodissociation regions (PDR) within the clumpy NGC 1333 cloud (Sandell & Knee 2001), as suggested by Spaans & van Dishoeck (2001). Second, near-infrared photometry has revealed a dense cluster of young stars embedded within the molecular gas (Aspin, Sandell, & Russell 1994; Lada, Alves, & Lada 1996; Aspin & Sandell 1997). These clustered young stars have powered a burst of energetic outflow activity manifested in the detection of clumps of vibrationally excited H₂ emission and a large number of Herbig-Haro objects (Aspin, Sandell, & Russell 1994; Bally, Devine, & Reipurth 1996; Hodapp & Ladd 1995). These clumps of high excitation are associated with a complex cluster of overlapping molecular outflows that dominate the structure in the dense core of the NGC 1333 molecular cloud and apparently have carved out large cavities within the dense gas (Langer, Castets, & Lefloch 1996; Lefloch et al. 1998; Knee & Sandell 2000). Thus, it is possible that the outflows have enriched the quiescent gas with water vapor, which is also a focus of this paper.

We report detections of spectrally resolved water vapor emission in several distinct outflows, and also from several positions tracing the quiescent gas. To aid in the analysis of the SWAS data, we present results from a supplementary survey of NGC 1333, using the Five College Radio Astronomy Observatory (FCRAO), in transitions of CO, ¹³CO, N₂H⁺, CH₃OH, and SiO. Our analysis of these combined data sets suggests that the quiescent water abundance is enhanced relative to cold pre-stellar molecular cores. Despite the pervasive presence of outflowing gas we find no supporting evidence that the quiescent water vapor is due to past shock episodes. Rather the correspondence between the water emission and high-J ¹³CO emission suggests that a PDR could provide additional heating to excite water in relatively low density quiescent gas. The observations and data reduction are presented in §2, and in §3 we present the results and a comparison of the integrated emissions maps with the water vapor distribution. In §4 we derive an estimate of the o-H₂O abundance in the high and low velocity gas. In §5 we discuss the origin of water vapor emission in NGC 1333. Our conclusions are given in §6.

2. Observations

The SWAS o-H₂O observations presented here were obtained during 678 hours between 1999 January – March, 1999, 1999 August, 2000 January – February, 2000 August – October, and 2002 January. The spacecraft was used in nod mode, involving alternately nodding the spacecraft to an off-source position free of emission ($\alpha_{off} = 03:28:07.9$, $\delta_{off} = +33:10:22$; J2000). All survey data were obtained with the center referenced to the position of SVS 13: $\alpha = 03:29:03.7$, $\delta = 31:16:02.7$ (J2000). Table 1 summarizes the specific positions surveyed, the total integration time, and the rms in the 557 GHz band. A total of 9 separate pointings were made, in some cases with the elliptical SWAS beam slightly overlapped. This survey is biased in that known centers of activity were specifically centered in the antenna beam (e.g. IRAS 2, 4, 7, and HH7-11). Additional observations were obtained offset from these targeted positions. Towards each position we have assigned a SWAS survey number (SS#; provided in Table 1) that is used for ease in reference in cases where there is no clear association with an existing well known source. Table 2 provides a listing of the line frequencies, beam size, and adopted main beam efficiency. All data were reduced with the standard SWAS pipeline described by Melnick et al. (2000b). Towards each offset position, along with o-H₂O, SWAS simultaneously observed transitions of [C I] ($^3P_1-^3P_0$), ^{13}CO ($J = 5-4$), and O₂ (3_3-1_2). In this work we primarily use the o-H₂O and ^{13}CO data, with a velocity resolution of 1.0 km s⁻¹, and a sampling of 0.6 km s⁻¹. Molecular oxygen was not detected towards any position down to a typical rms of $\sigma(T_A^*) = 42$ mK (3σ). With all data in the survey averaged together there is still no O₂ detection, with a 3σ upper limit of 12 mK.

Beam sampled maps of the mm-wave rotational transitions of ^{12}CO , ^{13}CO , C¹⁸O, N₂H⁺, HCO⁺, and SiO were obtained with the FCRAO 14 m antenna on 2000 November 12 and 13, and 2001 March 11 and 12. Pointing was checked frequently on the SiO masers (R Cas and Orion) with an accuracy of $< 4''$. Typical SSB system temperatures were 500 K (^{12}CO), 290 K (^{13}CO), 350 K (C¹⁸O), 200 K (N₂H⁺), 250 K (HCO⁺), and 200 K (SiO). Table 2 summarizes other relevant observational information. The maps encompassed the entire region surveyed by SWAS and covered a spatial region of nearly $17' \times 15'$. The SWAS and FCRAO data are presented here on the T_A^* scale and are uncorrected for antenna efficiency. All analysis is performed correcting for main beam efficiency, provided in Table 2.

3. Results

3.1. SWAS

We have obtained a wealth of additional higher resolution data to supplement the SWAS observations. These data are primarily used to place the SWAS observations in context with the general structure of the core. In this section we present only the integrated intensity maps of N_2H^+ $J = 1-0$ (Figure 1) and ^{13}CO $J = 1-0$ (Figure 2) to delineate the location of dense condensations and low density gas in NGC 1333. Figure 1 also provides the spectra of $\text{o-H}_2\text{O}$ $1_{01} - 1_{10}$ taken towards 9 positions in NGC 1333. The observed intensity, line center velocity, and velocity width of the $\text{o-H}_2\text{O}$ $1_{10} - 1_{01}$ detections are given in Tables 3 and 4. Relevant parameters for additional molecular transitions are also provided. In Figure 1 the dashed line in each spectra denotes the velocity of the quiescent gas determined through Gaussian fits to the N_2H^+ emission convolved to a simulated $4'$ circularized SWAS beam. The positions of the SWAS $\text{o-H}_2\text{O}$ observations, along with the elliptical SWAS beam given at the observed rotation angle, are shown superposed on the integrated emission map of N_2H^+ ($1-0$). N_2H^+ has been shown to be a good tracer of the dust distribution (Bergin et al. 2001; Tafalla et al. 2002), and in this case shows an excellent correspondence to the observed dust continuum emission (compare with Lefloch et al. (1998); Sandell & Knee (2001); see also Di Francesco et al. (2001)).

Figure 1 shows clear detections of broad ($\Delta v > 20 \text{ km s}^{-1}$) water vapor emission lines towards IRAS 2, IRAS 4, and HH 7-11 (SVS 13). Given the narrowness of the line observed in the direction of SVS 12 there is no evidence for water emission in the SVS 12 outflow. In the direction of IRAS 7 we detect relatively broad emission, $\Delta v \sim 8.5 \text{ km s}^{-1}$, consistent with an origin in the IRAS 7 outflow. In each case where outflow emission is detected, at the velocity of the ambient gas, there is evidence for absorption from foreground material. The coincidence of these observations with strong N_2H^+ emission suggests that there is indeed quiescent gas towards each line of sight. Water has previously been detected in IRAS 4 by ISO and SWAS, and HH7-11 by ISO¹ (Ceccarelli et al. 1999; Neufeld et al. 2000a; Molinari et al. 2000; Giannini, Nisini, & Lorenzetti 2001). We note that there is some beam overlap in these observations, particularly in the case of IRAS 2 and IRAS 7 with HH 7-11. However, for IRAS 2 and HH7-11 the $1_{10} - 1_{01}$ peak flux is comparable (Figure 1), which would not be the case if either detection is the solely the result of contamination from the other. Thus,

¹The spectrally unresolved ISO detections of high lying H_2O transitions can also be interpreted as arising from envelope gas in proximity to IRAS4a,b (Ceccarelli et al. 1999). However, the spatially unresolved, but spectrally resolved, SWAS observations clearly demonstrate that emission in the 557 ground state, at least, predominantly arises within the outflow (Neufeld et al. 2000a).

it is likely that SWAS has detected water emission from both flows. In the case of IRAS 7 it is possible there could be some contribution from an extended HH7-11 flow. As this is currently uncertain we assume all the emission arises solely from IRAS 7.

For 3 positions, SS1, SS2-SVS 12, and SS5, there are significant detections of a narrow, $\Delta v \sim 2 - 3 \text{ km s}^{-1}$, component of o-H₂O emission associated with cold dormant material. In each case the emission is blue-shifted with respect to the systemic velocity as defined by C¹⁸O (compare Gaussian fit line center velocities in Table 4) and N₂H⁺. There is no clear correlation of the ambient water emission to the dense condensations traced in N₂H⁺, as only the SVS 12 (SS2) observation coincides with a dense clump. Indeed the water emission towards SS5 lies inside the well known cavity between SVS 12 and SVS 13 (Warin et al. 1996; Langer, Castets, & Lefloch 1996; Lefloch et al. 1998; Sandell & Knee 2001).

In Figure 2 we provide the observed spectra of the J = 5–4 transition of ¹³CO, while Table 5 lists the integrated intensity and line parameters. Similar to Fig. 1, we show the beam positions of the SWAS observations placed on a map of the ¹³CO J = 1–0 integrated emission. The J = 5–4 SWAS observations were obtained simultaneously with H₂O and have identical pointing. Clearly the strongest ¹³CO J = 5–4 emission, by nearly a factor of two, is not associated with the more well known molecular cores, such as HH7-11, IRAS 2, or even IRAS 4. Rather this strong emission is seen towards SS1 and SS2-SVS12, which are close to the known sources of reflection nebulosity, BD +30.549 and SVS 3. These sources are likely heating the nearby gas in the PDR, which excites high-J emission lines. The SWAS observations towards these two positions also overlap the strongest clump of ¹³CO J = 1–0 emission. However, the ¹³CO J = 1–0 emission maximum does not correlate with with any dense condensation as traced by N₂H⁺ (compare Figures 1 and 2).

The 2 positions with strong J = 5–4 emission also coincide with 2 detections of quiescent o-H₂O. However, quiescent H₂O is also seen towards SS5, which has moderate intensity ¹³CO J = 5–4 emission in comparison to other positions. The association of strong J = 5–4 emission and the presence of the nearby luminous sources, along with a partial correlation with detections of quiescent o-H₂O, suggests that the presence of a photodissociation region (PDR) in the northern portions of NGC 1333 may be related to the presence of quiescent water emission. This question is investigated in §5.

3.2. FCRAO

Within the central portion of the NGC 1333 core lie a number of individual objects and systems (SVS 13, IRAS 2, IRAS 4) and their associated outflows that have been the subject

of a multitude of molecular investigations (Snell & Edwards 1981; Bachiller & Cernicharo 1990; Sandell et al. 1994; Blake et al. 1995; Warin et al. 1996; Langer, Castets, & Lefloch 1996; Lefloch et al. 1998; Codella, Bachiller, & Reipurth 1999; Di Francesco et al. 2001; Rudolph et al. 2001). However, these investigations generally focused on individual sources and most of the molecular transitions have not previously been observed over a large scale in the unbiased fashion required for this study. The detection of abundant SiO in the ambient gas in NGC 1333 (Lefloch et al. 1998; Codella, Bachiller, & Reipurth 1999) has particular relevance to any o-H₂O ambient emission. SiO is rarely detected in cold material (Ziurys, Friberg, & Irvine 1989; Codella, Bachiller, & Reipurth 1999); rather it appears to be found predominantly in hot shocked material (Bachiller 1996). The origin of SiO in shocks is believed to originate from the release of silicon from grain cores by ablation in shocks, followed by gas-phase chemical reactions (Schilke, Walmsley, Pineau Des Forets, & Flower 1997; Caselli, Hartquist, & Havnes 1997; May et al. 2000). The quiescent SiO in NGC 1333 could originate from previous shock episodes or through current interactions with the dense condensations (Lefloch et al. 1998; Codella, Bachiller, & Reipurth 1999). It is also well known that the abundance of CH₃OH is enhanced in outflows (Bachiller 1996), and broad emission components have been detected in IRAS 2 and 4 (Sandell et al. 1994; Blake et al. 1995). As such, a shock origin that created SiO in the ambient gas could be operative for both H₂O and CH₃OH.

In Figure 3 we show a sample of the spectra taken from all species and transitions in the survey towards HH7-11, IRAS 4, and SS5. The data is shown on a relative intensity scale and are used to convey how each species traces the high and low velocity dispersion gas. The spectra are representative of the FCRAO data in this study, and are shown at the observed resolution provided in Table 2. Towards HH7-11 and IRAS 4 we find clear detections of high velocity emission in CO, HCO⁺, and o-H₂O and there is evidence for emission from the low velocity dispersion quiescent gas in nearly every tracer. In IRAS 4 we detect the emission of quiescent SiO seen earlier by Lefloch et al. (1998) and Codella, Bachiller, & Reipurth (1999). In the following we present the distribution of these tracers separately and, more specifically, discuss how it compares to the SWAS data.

The emission distribution of the high velocity CO gas has been studied in detail by Knee & Sandell (2000), with higher resolution than obtained in this study. However, for completeness, in Figure 4 we provide the distribution of the blue-shifted and red-shifted (with respect to the systemic velocity) CO emission from the outflowing gas (left-hand panel) along with a similar plot for HCO⁺ (right-hand panel). In both molecules the emission is dominated by the HH 7-11 outflow. This flow is centered on SVS 13 and fills the cavity above SVS 13 (Knee & Sandell 2000). Weaker emission towards other sources (IRAS 4, IRAS 2, IRAS 7, and SVS 12) is seen as slight extensions in the contours of this flow. Each

of the outflows are seen much more prominently in the higher resolution IRAM data of Knee & Sandell (2000).

Figure 5 presents integrated intensity maps for the CO isotopes, ^{13}CO and C^{18}O . These maps are broadly similar to the lower resolution C^{18}O maps of Warin et al. (1996). In particular, the cavity between SVS 13 and SVS 12 is quite prominent. A close comparison of the C^{18}O emission distribution with the N_2H^+ morphology presented in Figure 1 shows that the C^{18}O integrated intensity peaks do not coincide with the strongest N_2H^+ features. Since N_2H^+ closely traces the dust emission, C^{18}O is probably depleted in the densest portions of the NGC 1333 core, and therefore provides an underestimate of the total column density. In the following we adopt C^{18}O as a tracer of total column density of quiescent material and the effects of depletion on the derived abundances is discussed in §5.

In Figure 6 we present the observed emission distributions for SiO (top) and CH_3OH (bottom), in both the high (right panels) and low (left panels) velocity dispersion gas. The right-hand panels show that SiO and CH_3OH are both detected in the IRAS 2 and IRAS 4 outflows. In our observations there is also weak CH_3OH emission in the HH7-11 outflow. In the $50''$ FCRAO beam we see no evidence for SiO emission in HH7-11; however, higher resolution observations have detected SiO in this outflow (Codella, Bachiller, & Reipurth 1999). Thus, albeit with the limited statistics available in this sample, there is some correspondence between the clearest SWAS detections of $\text{o-H}_2\text{O}$ in molecular outflows (IRAS 2, 4, and HH7-11) and the presence of methanol and silicon monoxide. A similar relation between SiO and H_2O has been suggested by Nisini et al. (2000) in a study of the L1448 outflow, but see also Ceccarelli et al. (1999). There does not appear to be any CH_3OH or SiO associated with the IRAS 7 or SVS 12 outflows.

The SiO narrow component (top, left panel) emission is found predominantly between IRAS 2, IRAS 4, and SVS 13. The previous SiO observations of Lefloch et al. (1998) covered an area of $\sim 2'.2 \times 4'.3$ centered approximately between IRAS 4 and SVS 13. The larger scale observations presented here reveal one new clump of ambient SiO emission located to the north of IRAS 7. The clump in the vicinity of IRAS 2 is contaminated by outflow emission. We find no evidence for ambient SiO emission directly coincident with the 3 SWAS detections of quiescent water in *emission* (SS1, 2, 5). Given the observed distribution, the narrow component SiO could still be associated with the water seen in absorption towards each of the outflows. The CH_3OH narrow component (bottom, left panel) is more distributed throughout the core, with the strongest emission clustered near SVS 13, IRAS 4, and IRAS 2. The comparison of CH_3OH with SiO shows some similarities, particularly between SVS 13 and IRAS 4, although the clump near IRAS 2 is also contaminated by outflow emission (similar to SiO). However, there are 2 clumps of methanol emission in the northwest that

are not observed in SiO. Thus, there is some, but not convincing evidence of a shock origin for ambient CH₃OH. In relation to the o-H₂O observations, there is no evidence for CH₃OH emission directly associated with SS1 and it is only weakly seen in the cavity (SS5; Figure 3). In addition, there is no H₂O emission towards SS3, a position coincident with a CH₃OH clump.

3.3. Summary of Emission Correlations

In this section we briefly summarize the correlations between the emission distributions of various tracers discussed above. It is important to note that molecular emission does not necessarily directly trace any given physical variable, because a change in molecular concentration and/or cloud physical properties (temperature, density, clump filling factor) result in changes in emission. However, dust emission, and by association N₂H⁺, clearly delineate the presence of dense condensations in the NGC 1333 molecular core and we find no clear connection of quiescent water emission detections with these tracers. Similarly, the mere presence of SiO in the quiescent gas is an indicator of a shock chemistry “legacy” in the ambient medium and the quiescent water emission shows no association with narrow component SiO emission. In fact, the detections of water in absorption may trace similar gas. Finally, 2 of the 3 detections of quiescent water emission are towards positions with unusually strong ¹³CO J = 5–4 emission.

4. Analysis and o-H₂O Abundance Determinations

In the previous section we used the higher resolution FCRAO data to examine the relation between the observed distribution of water vapor to other tracers. We have detected water vapor in 3 distinct regimes: (1) broad emission associated with outflows, (2) narrow emission associated with the quiescent gas, and (3) absorption by foreground quiescent gas against the outflow emission. In the following we make estimates of the water vapor abundance for each in turn. This analysis is complicated by the fact that the SWAS beam is large when compared to the size scale of structures, either outflow or clumpy substructure within NGC1333. In addition, to determine abundances with observations of a single H₂O transition requires knowledge of the density and temperature structure over a large portion of the NGC 1333 molecular core. These values can be estimated via multitransitional studies, but are themselves averages of structures within a telescopes beam and along the line of sight. The difficulties in this process have been discussed previously by Snell et al. (2000a) and Neufeld et al. (2000a). Fortunately, for this particular core we can draw upon the wealth

of data obtained previously, and for this study, to derive simple estimates, or limits, on the average water abundance within a SWAS beam.

4.1. Water Abundance in the Outflows

Based on the distribution of CO and HCO⁺ emission, the outflows, except HH7-11 are confined to regions smaller than the SWAS beam. Thus, one uncertainty in deriving the o-H₂O abundance is the unknown filling factor of water emission. The SWAS water emission could be confined to a series of small shocked HH knots such as seen in the ISO water detections by Molinari et al. (2000). Indeed the SWAS observations in Figure 1 overlap with a number of HH objects and we have not placed on this figure the objects with HH like nebulosities (Aspin, Sandell, & Russell 1994; Hodapp & Ladd 1995), which would increase the correspondence. Alternately, the emission might arise from a similar region traced by the high velocity emission of other molecular tracers such as CO, CS, SiO, or CH₃OH. We treat each of these possibilities in turn.

4.1.1. Shock Origin

To explore the likelihood that *all* of the water emission seen by SWAS arises in the shocked gas (not the extended molecular outflow seen in CO), we have used the non-dissociative C-shock models of Kaufman & Neufeld (1996) (hereafter KN96). In these models the strength of 557 GHz water emission within a SWAS beam depends on the shock velocity, pre-shock density, filling factor of shocked gas within the beam, and gaseous oxygen abundance, along with other parameters (ionization fraction, magnetic field strength). With suitable assumptions regarding the ionization fraction and magnetic field strength (see KN96) we have run a grid of shock models encompassing shock velocities of 10, 15, and 20 km s⁻¹ for pre-shock density of n_{H₂} = 10⁵ cm⁻³. We also examined an additional model with $v_{shock} = 15$ km s⁻¹ and a pre-shock density of n_{H₂} = 10⁴ cm⁻³. In each model the water abundance is determined by the assumed abundance of atomic oxygen. The H₂O is produced solely through gas-phase neutral-neutral reactions and not by grain mantle sputtering of H₂O. This will not affect the results, as the main dependence is on the final water abundance and not the exact mechanism.

For this analysis we use corollary ISO observations of the o-H₂O 2₁₂ – 1₀₁ 179 μm line. Briefly, ISO has detected 179 μm water emission within a ~80'' beam towards IRAS 4 and, with a lesser degree of certainty, IRAS 2 (Ceccarelli et al. 1999). Observations towards

off-source positions coincident with outflow peaks found weak or insignificant detections (Giannini, Nisini, & Lorenzetti 2001; Maret et al. 2002). Molinari et al. (2000) detailed ISO observations of the HH7-11 flow, where 179 μm o-H₂O emission was detected towards HH7 and SVS 13 (HH11 and HH10 in the beam). There were no detections towards the red lobe peaks in the molecular outflow seen in other tracers. In Table 3 we provide the total integrated emission strengths for the 557 GHz line and total fluxes for each source in the 179 μm line.

Our shock model analysis, when compared to both ISO and SWAS data, provides one general result. We are able to reproduce the observed 179 μm flux in the weakest shock in our sample, with a pre-shock density of $n_{\text{H}_2} = 10^4 \text{ cm}^{-3}$ and a shock velocity of 15 km s^{-1} . Even though the weakest shock reproduces the 179 μm emission it does not explain the SWAS emission. If we assume a typical HH object has a size of 10'' (based on the extent of H₂ (1-0)S(1) emission in HH7; Molinari et al 2000), then a single object produces $\int T dv(\text{o-H}_2\text{O } 1_{10} - 1_{01}) \sim 0.38 \text{ K km s}^{-1}$. Adding additional shocks aids in matching the SWAS data, but exceeds the ISO observations. Thus, it is likely that the SWAS emission is not from the shock itself, but rather from cold post-shock gas. Colder temperatures allow for increases in the 557 GHz emission, without augmenting the 179 μm flux. Molinari et al. (2000) found similar problems when comparing shock models to the ISO data, which might therefore be reconciled through the addition of a cold water component with elevated abundances in the high velocity gas. This conclusion gains additional support through the combined ISO and SWAS study of four outflows by Benedettini et al. (2002), who find that the SWAS 557 GHz emission receives a strong contribution from cold gas that is not traced by ISO.

4.1.2. *Post-Shock Origin*

The results from shock models suggest that the 557 GHz observations could be primarily tracing cold gas, in a manner potentially similar to that seen by other molecules such as CO, CS, CH₃OH, and SiO. Clearly this is an over simplification, as some small fraction of the emission seen by SWAS must originate from the hot gas detected by ISO. However, it does allow for simple limits to be set on the abundance. One complication is that the various molecules have disparate distributions within the SWAS beam (see Figures 4 and 5), each with its own filling factor. To establish a lower limit to the abundance, we assume that the water is tracing the same gas seen in low-J CO emission, which has the most widespread emission and greatest filling factor. An estimate of the water abundance can be derived with knowledge of the density, temperature, and column density structure, within the outflow. In Table 3 we list our assumptions for these properties, which are justified below.

Since we have assumed that o-H₂O is tracing the same gas seen in CO line wings, we use the CO high velocity emission to estimate the total gas column density. The H₂ column density is then derived from the CO column density given in Table 3 and $n_{\text{CO}}/n_{\text{H}_2} = 10^{-4}$. Density estimates in several of the NGC 1333 outflows can be found in the literature, typically based on observations of several transitions of CS. Rather than adopting values from the literature, we have performed our own multi-transitional fit using the CS J=2–1, 3–2, and 5–4 data of Langer, Castets, & Lefloch (1996) and Lefloch et al. (1998) that has been kindly provided to us by the authors. These data were obtained with the IRAM 30m with angular resolutions of 25'', 16'', and 10''. Before performing the excitation analysis we convolved all data to the lowest resolution. Each of these maps was sampled with a spacing of 24'' on the cloud, and 12'' near the IRAS 2 and 4 outflows. Thus some information is missing from the convolution for the CS J=5–4, and to a lesser extent, the J = 3–2 observations. To extract the outflow emission from the ambient emission, the CS J=2–1 data for each position were fit with a multi-component Gaussian. The same process was performed for the CS J=3–2 and J=5–4 data. However, for each position the line center velocity and velocity width were fixed to the multi-component values derived from CS J=2–1 and only the peak intensity was allowed to vary. This was done both for the outflow and quiescent emission components. The procedure produced good fits to the data for nearly all positions.

The results of this process are the integrated fluxes from the broad emission component fit with the same linewidth for all 3 CS transitions at every position with significant outflow J=2–1 emission. These data were then fit using a LVG excitation code for CS excitation in the manner described in Bergin, Snell, & Goldsmith (1996). CS emission is generally optically thick in molecular clouds. However in our analysis the spread of emission in frequency due to the molecular outflow reduces the opacity. Our model is then simply a fit to the excitation of the rotational ladders in statistical equilibrium. For consistency we adopt a constant temperature for each outflow using the values given in Table 3. In this fashion, densities, with constant temperature, are derived as a function of position where high velocity CS J=2–1 was detected. For each outflow these densities are averaged together, weighted by the errors, resulting in a single average density for each of the 4 outflows. These densities are slightly lower than quoted in the literature (Langer, Castets, & Lefloch 1996; Rudolph et al. 2001) due to our convolution to a uniform resolution and the detailed Gaussian fitting process.

With the average physical quantities provided in Table 3 we derive a simple estimate of the water abundance, under the assumption that the water emission is optically thick, but effectively thin (see Snell et al. 2000 and Neufeld et al. 2000). Under this assumption every collisional excitation results in a photon that eventually escapes the cloud, which is possible when the density is significantly below the critical density for excitation. This condition

is satisfied on average for each of the flows. In this case, for effectively thin emission, the average column density of o-H₂O within a SWAS beam is related to the 557 GHz line strength by:

$$N(\text{o-H}_2\text{O}) = \frac{4\pi}{hc^3} \frac{2\nu^2k}{C_{ul}n_{\text{H}_2}} e^{(h\nu/kT)} \int T_{\text{R}} dv \quad (1)$$

where C_{ul} is the downwards collisional rate of o-H₂O with ortho and para-H₂. Rates of excitation of water with ortho-H₂ are often an order of magnitude greater than rates for lower energy para-H₂ (Phillips, Maluendes, & Green 1996). Thus assumptions regarding the H₂ ortho/para ratio are required to derive water abundances and introduce an additional source of uncertainty. As in Neufeld et al. (2000a) we assume that all H₂ is in the ground rotational state. Table 3 provides the column density of o-H₂O in the outflows and the water abundance is calculated using the CO column density. The values derived range from 4×10^{-7} to 1×10^{-6} . The value estimated for IRAS 4 is slightly below that found by Neufeld et al. (2000a), due to different assumptions regarding the density and total column density (mass) in the outflow. Towards HH7-11 there is evidence in the high signal to noise ¹³CO J = 5–4 detection of a broad emission component below the narrow quiescent gas emission. This broad emission component can be used to set limits on the column density of warm gas within the SWAS beam and has an integrated emission of 0.43 ± 0.04 K km/s. Using the physical parameters for HH7-11 in Table 3 we estimate a CO column density of $\sim 1 \times 10^{16}$ cm⁻² is required. This value is quite comparable to that estimated for “hot” CO gas by Molinari et al. (2000) ($N(\text{CO}) \sim 10^{16}$ cm⁻²). Thus, if all the 557 GHz water emission arises from the same gas as traced by this component then the abundance is $x(\text{o-H}_2\text{O}) \sim 8 \times 10^{-6}$.

Equation (1) will also hold for the 2₁₂ – 1₀₁ transition of o-H₂O observed with ISO. Using the densities and temperatures listed in Table 3 and the column density that matches the observed 1₁₀ – 1₀₁ emission we can predict the amount of water emission at 179 μm. These predictions are also provided in Table 3 and are nearly two orders of magnitude below the observed values. This confirms the earlier assertion that a single model cannot account for the emission of both lines and that the 557 GHz emission likely traces cold post-shock gas. The 179 μm emission preferentially probes either warm shocked gas, such as seen in HH7, or, the warm envelopes surrounding protostars, as proposed by Ceccarelli et al. (1999) and Maret et al. (2002).

The abundances provided in Table 3 are averaged over the outflow and are based on a data set analyzed with consistent assumptions for each flow. They represent a lower limit to the actual water abundance in the high velocity gas, which is due to a number of factors. (1) If the water emission is not effectively thin then using equation (1) leads to an underestimate

of the total column density. (2) We have made the conservative assumption that the o-H₂O emission traces that of CO. Thus, the average abundances do not rule out spatial variations in the water vapor distribution within a SWAS beam. Such a distribution would exist if the SWAS observations were probing the hot shocked regions seen in ISO and any additional colder component. This is supported by the large velocity widths of the o-H₂O emission when compared to CO (Table 3). (3) Under the effectively thin approximation the greatest uncertainty in the abundance lies in the determination of the density of molecular hydrogen. We have assumed that the entirety of the outflow traced in high velocity CO emission is uniformly filled with gas at a density of $\sim 10^5$ cm⁻³. This is likely not the case as, within a given SWAS measurement, emission from the dense gas tracers, such as CS and HCO⁺, are more spatially confined when compared to CO.

4.2. Water Abundance in the Quiescent Gas

Similar to outflow emission, the water abundance calculation for the quiescent component is complicated due to structure within the large SWAS beam. Furthermore, the line intensity distribution of typical tracers of the dense gas, such as dust continuum, N₂H⁺, and CS emission do not consistently agree with the water distribution. SS5 lies within a cavity generally (although not completely; Figure 3) devoid of emission from each of these tracers, and there is little dust continuum or N₂H⁺ emission towards SS1. For detections of water emission we therefore compute beam-average abundances in a fashion similar to §4.1.

For the quiescent gas, the density is well below critical (Langer, Castets, & Lefloch 1996), and the water emission is optically thick, but effectively thin. For the temperature we use the observed ¹²CO excitation temperature towards each position determined from the J=1–0 map of spectra convolved to a circularized 4' SWAS beam. This value is generally ~ 20 K. To derive the total column density, the C¹⁸O J=1–0 data is also convolved to 4'. The total column density is estimated from the integrated intensity, assuming LTE at the CO excitation temperature and a C¹⁸O fractional abundance of 1.7×10^{-7} .

The density estimate is complicated by the lack of emission from tracers of the dense gas at positions near the quiescent H₂O detections. We therefore use the ratio of the SWAS ¹³CO J=5–4 to FCRAO ¹³CO J=1–0 (convolved to 4') as our primary density estimate. Figure 7 shows the ¹³CO 5–4/1–0 ratio as a function of density and ¹³CO opacity for a temperature of 20 K. This ratio is strong function of density and, with knowledge of the opacity (using the ¹³CO/C¹⁸O ratio assuming ¹²C/¹³C = 60 and ¹⁶O/¹⁸O = 500) and temperature, can be used to provide an estimate of the average density within a 4' beam. Using these average properties, an H₂ ortho/para ratio thermalized at 20 K and Eqn. (1) we derive single

component beam-average abundances which are listed in Table 4 along with the other derived quantities.

The water abundances are uniform at a value of $\sim 1 \times 10^{-7}$. The primary uncertainty in this calculation lies in the density determination. Here we have adopted ^{13}CO as our density tracer. ^{13}CO has a low dipole moment and is much more easily excited in the low density gas than $\text{o-H}_2\text{O}$. Thus its emission, particularly for $J=1-0$, contains a contribution from the low density gas that should not participate in the excitation of H_2O molecules. This would increase the density, and decrease the water abundance. Therefore, it is unlikely that the average density within the beam is much lower than our adopted value and, provided the temperature is not much higher than 20 K, our abundances represent upper limits. A lower abundance limit can be set by examining the distribution of other dense gas tracers within the SWAS beam. The detection of ambient $\text{o-H}_2\text{O}$ emission in SVS 12 is coincident with a clump of N_2H^+ emission, which traces gas with $n_{\text{H}_2} > 10^5 \text{ cm}^{-3}$. It is clear from Figure 1 that the dense gas does not fill the SWAS beam. If we convolve the N_2H^+ FCRAO data towards this position to a resolution of $4'$, we find an N_2H^+ opacity ~ 1 and excitation temperature ~ 4 K. From a LVG excitation model these values are roughly coincident at a density $\sim 10^5 \text{ cm}^{-3}$, and the range of beam-average density lies between $10^4 - 10^5 \text{ cm}^{-3}$. This limits $\text{o-H}_2\text{O}$ abundance that corresponds to these densities ranges from $0.1 - 1 \times 10^{-7}$.

4.3. Absorption by Foreground Quiescent Gas

The detections of quiescent water in absorption against outflow emission (§ 3) can be subject to a more simplified analysis. As seen in Figure 1 none of the absorption features reach the continuum-subtracted baseline. Thus at the 1σ level the absorption lines are not saturated. This could be the result of optically thin emission or, alternately collisionally excited water in the surrounding dense gas could fill in the absorption trough. If we assume the line is resolved and unsaturated, only a small column density of water is required to absorb 557 GHz emission, and these small absorption features can be reproduced by an $\text{o-H}_2\text{O}$ abundance relative to H_2 of only 6×10^{-11} . However, each of the absorption features is consistent, at the 3σ level, with saturation, in this case the abundance is a lower limit. Therefore these measurements do not place stringent limits on the ambient water abundance.

5. Discussion

To examine the origin of the quiescent water emission in NGC 1333 we can first compare the o-H₂O abundance in NGC 1333 with those determined towards other sources by Snell et al. (2000a) and Bergin & Snell (2002). First it is clear that the quiescent ortho-water abundance in NGC 1333 is greater than that found in cold star-less clouds. For instance in TMC-1 the o-H₂O abundance relative to H₂ is $< 7 \times 10^{-8}$ (Snell et al. 2000a). More stringent limits ($x(\text{o-H}_2\text{O}) < 1 - 7 \times 10^{-9}$) have been set towards B68 and ρ Oph Core D (Bergin & Snell 2002). These two cores have well described physical properties providing more accurate abundance determinations. In NGC 1333 the lower limit to the quiescent water abundance (1×10^{-8}) is well above the upper limits found in B68 and ρ Oph D. Similarly, on average, the quiescent water abundance in NGC 1333 appears to be higher than derived towards denser and more massive star-forming cores such as OMC-1 or M17 where abundances range from $0.1 - 1 \times 10^{-8}$ (Snell et al. 2000b,c). However, it is comparable to values derived in low density clouds along the line of sight towards Sgr B2 and Sgr A* (Cernicharo et al. 1997; Neufeld et al. 2000a; Moneti, Cernicharo, & Pardo 2001).

One concern is the use of C¹⁸O as a column density tracer in our calculation, and in the previous abundance estimates. In NGC 1333 C¹⁸O appears to be depleted and the primary effect of this depletion would be to raise the o-H₂O abundance. If C¹⁸O depletion is more significant in NGC 1333 than in B68 or ρ Oph D then the abundance disparity could be reconciled. However, this is unlikely as the colder clouds should have more significant C¹⁸O depletion, and hence higher abundances. In sum it appears that the water abundance in NGC 1333 is enhanced, certainly when compared to colder pre-stellar molecular cores. Herschel observations of ortho and para forms of water, and additional transitions, in the ambient gas will provide the data to confirm or refute this result.

Given the widespread nature of outflow activity, the quiescent water abundance enhancement in NGC 1333 could be the result of gas exposure to numerous shocks. Indeed in §4.1 we found evidence that the water in the high velocity gas is likely cold and therefore has begun the process of enriching the surrounding gas with cold water vapor. However, through our analysis of other tracers of shock activity (SiO and CH₃OH), we find little or no evidence to support this assertion. All positions where quiescent water emission is detected (SS1, SS2-SVS12, SS5) show no quiescent SiO emission and only 1 position coincides with strong CH₃OH emission. Thus, despite the appeal, this hypothesis has no support from the molecular data.

However, quiescent H₂O emission is correlated with detections of unusually strong ¹³CO J = 5–4 emission. This emission is in close proximity to the nearby B stars (BD +30.549 and SVS 3) that power the reflection nebula. This region has been identified as a PDR

through observations of infrared emission arising from PAHs (Joblin, Tielens, Geballe, & Wooden 1996; Uchida, Sellgren, Werner, & Houdashelt 2000). PDR’s are characterized in terms of the enhancement of the FUV field, G_0 , measured in units of the equivalent flux of $1.6 \times 10^{-3} \text{ ergs cm}^{-2} \text{ s}^{-1}$ determined by Habing (1968) for the interstellar medium. The stellar luminosities for these stars are given by Harvey, Wilking, & Joy (1984) (BD +30.549: $400 L_\odot$; SVS 3: $360 L_\odot$), with these values we estimate $G_0 \sim 400$ towards the two northernmost SWAS survey positions (SS1, SS2-SVS12) and $G_0 \sim 100$ towards SS5. These FUV enhancements provide additional heating that excites the high-J lines of ^{13}CO that we observe. The strongest ^{13}CO $J = 5-4$ emission arises in lower density gas closest to the interface and will have the largest FUV enhancements (e.g. SS1, SS2). However, ^{13}CO $J = 5-4$ emission is also observed throughout the NGC 1333 cloud (e.g. Figure 2). Towards SS6-8 (HH7-11, IRAS 2, IRAS 4) this emission is coincident with dense condensations traced with N_2H^+ , thus the higher density, and embedded protostars, provide added excitation to account for any reduction in heating from the external FUV field.

Given the evidence for enhanced FUV radiation we have explored whether a PDR could give rise to the observed o- H_2O emission, as suggested by Spaans & van Dishoeck (2001). The PDR calculations presented here are from the model of Tielens & Hollenbach (1985), updated by Kaufman et al. (1999). The model self-consistently calculates the temperature and equilibrium chemical structure of gas illuminated by far-ultraviolet radiation from nearby stellar sources, given the FUV field strength G_0 and the gas density, and outputs the expected line intensities from atomic and molecular species. In the outer, atomic regions ($A_V \lesssim 3-5$), cooling is primarily through far-infrared emission from CII and OI, while further in ($A_V \gtrsim 5$) cooling by molecular species such as CO and ^{13}CO becomes important.

In our plane-parallel geometry for the PDR model we fix the depth to 11 mag by the observed C^{18}O column density (scaled by the C^{18}O abundance). This is clearly an approximation as the true extinction between the external sources and the water emitting gas is unknown. We assume $n_{\text{H}_2} = 2 \times 10^4 \text{ cm}^{-3}$ based on the multi-transitional ^{13}CO analysis. To predict the water abundance profile we use the time-dependent gas-grain chemical model of Bergin et al. (2001) using the same density and the gas temperature profile as in the PDR calculations. We adopt the new H_3O^+ dissociative recombination branching ratios of Neau et al. (2000). Models with these parameters were run for values of $G_0 = 1, 100,$ and 400 , predicting the fluxes from ^{13}CO $J = 5-4$ and o- H_2O $1_{10} - 1_{01}$. Figure 8 presents the model gas temperature and water abundance profile, along with the integrated emission as a function of extinction. Table 6 provides the average abundances and integrated fluxes from the model.

The H_2O abundance is reduced at low extinction due to photodestruction and rises

towards higher extinction as the UV photons are absorbed by dust grains. Because the gas is at relatively low density we have assumed that the water molecules have not yet had sufficient time to freeze out as in dense cores. For $n_{H_2} = 2 \times 10^4 \text{ cm}^{-3}$, models with $G_0 = 1$ do not produce significant o-H₂O $1_{10} - 1_{01}$ or ¹³CO $J = 5-4$ emission. When the FUV field is raised, the line fluxes increase, and for $G_0 \geq 100 - 400$ the model reproduces both the quiescent H₂O and high-J ¹³CO observations. In cases with enhanced UV fields the average water abundance is $x(\text{o-H}_2\text{O}) \sim 1.5 \times 10^{-7}$ (assuming ortho-H₂O/para-H₂O = 3). This is close to the derived quiescent water abundance suggesting that simple gas phase chemistry in a PDR may be enough to account for the SWAS observations.

In all, the details are certainly more complex than included in the model presented here. However, additional support for the presence of an active PDR is found in the ISO detections of [C II] 158 μm and [O I] 63 and 145 μm emission towards the HH7-11 flow. Molinari et al. (2000) provide fluxes of $21.3 \times 10^{-20} \text{ W/cm}^{-2}$ ([C II] 158 μm), $180 \times 10^{-20} \text{ W/cm}^{-2}$ ([O I] 63 μm), and $8.0 \times 10^{-20} \text{ W/cm}^{-2}$ ([O I] 145 μm) towards SVS13. Assuming a higher density of 10^5 cm^{-3} for this gas (§4), the PDR models can reproduce the flux and flux ratios of these lines provided $G_0 \sim 50 - 100$. From the luminosities of the external sources and the relative distances to SVS13 we estimate $G_0 \sim 70$, consistent with the PDR model. Thus the model and available data are both suggestive of the importance of the PDR in NGC 1333 for creating the observed atomic and quiescent water emission.

The excitation of water in a PDR may therefore account for the water emission seen by SWAS towards other massive star forming regions, such as OMC-1 and M17. This may also account for the remarkable similarity in the spectral line profiles between o-H₂O $1_{10} - 1_{01}$ and CO $J = 2-1$ noted by Ashby et al. (2000). We stress that this is not in conflict with the oxygen freeze-out models of Bergin et al. (2000), because freeze-out is still required to account for the lack of a stronger signature in the water emission from gas that is clearly associated with regions of higher density, $n_{H_2} > 10^5 \text{ cm}^{-3}$ (i.e. the OMC-1 core). Here the water would be depleted in the dense regions, but not in the low density outer layers with longer depletion timescales and higher temperatures.

6. Conclusions

We have presented the results of a biased survey for $1_{10} - 1_{01}$ emission from o-H₂O in the core of the NGC 1333 molecular cloud using the Submillimeter Wave Astronomy Satellite. This survey is biased in the sense that known centers of activity were centered within the $3'.3 \times 4'.5$ SWAS beam. These data are supplemented by an unbiased FCRAO survey in the $J=1-0$ transitions of ¹²CO, ¹³CO, C¹⁸O, N₂H⁺, HCO⁺, and the $J=2-1$ transition of SiO.

Each of these transitions were mapped, with beam sampling, over an area that encompasses all SWAS observations. The primary results are listed below.

(1) We report the detection of broad o-H₂O emission in the IRAS 2, IRAS 7, and HH7-11 outflows. The detection of 1₁₀ – 1₀₁ emission in the IRAS 4 flow has been reported previously (Neufeld et al. 2000a). In each case the emission is accompanied by narrow absorption features at the quiescent cloud velocity. Towards 3 positions we detect narrow ($\Delta v < 3 \text{ km s}^{-1}$) emission clearly associated with the quiescent gas.

(2) Using these data sets we derive beam-averaged abundances for outflow emission in NGC 1333. In the outflows the water abundance relative to H₂ is $> 10^{-6}$. These abundances are averaged within the large SWAS beam and, hence, we have no information on structures smaller than 4'. However, with this caveat in mind, our results confirm the enhancement of o-H₂O in the NGC 1333 molecular outflows. A combination of published observations, and those reported here, find broad emission in SiO and CH₃OH in the HH7-11, IRAS 2, and IRAS 4 outflows. These same sources are the strongest centers of o-H₂O outflow activity detected by SWAS. Although the sample is quite limited, this is suggestive of a potential correlation between regions with SiO and CH₃OH abundance enhancements and detectable water emission. Models of non-dissociative (C-type) shocks are used to constrain the origin of the 557 GHz outflow emission seen by SWAS and 179 μm emission detected by ISO. These models suggest that the water abundance is enhanced within the shocks, but fail to reproduce the water emission unless the majority of the 1₁₀ – 1₀₁ emission arises from cold post-shock gas within a portion of the extended outflows.

(3) In the quiescent gas beam-averaged abundances lie between $0.1 - 1 \times 10^{-7}$. The quiescent water emission is correlated with unusually strong ¹³CO J = 5–4 emission and is found near the NGC 1333 reflection nebula and PDR. Through a PDR model we find that the local enhancements of the FUV field increase the gas temperature in relatively low density gas ($n_{\text{H}_2} \sim 10^4 \text{ cm}^{-3}$) allowing for simple gas phase chemistry (with slightly lower gas phase abundances due to photodissociation) to account observed fluxes in both ¹³CO J = 5–4 and o-H₂O 1₁₀ – 1₀₁. These results are consistent the results of Spaans & van Dishoeck (2001) who examined water emission in S140. Thus the excitation of water in low density gas, that is undepleted due to longer depletion timescales and exposed to local enhancements of the FUV field, may account for the extended 557 GHz water emission found towards a variety of molecular sources. However, depletion of oxygen in the form of water is still required for regions with significant amounts of dense gas along the line of sight.

This work was supported by NASA's SWAS Grant NAS5-30702. The Five College Radio Astronomy Observatory is operated with the support of the National Science Foundation

under grant AST01-00793. EAB is grateful to helpful discussions with C. Ceccarelli and S.T. Megeath, and to B. Lefloch and A. Castets for providing the multitransitional CS data. We also are grateful to the referee for providing a thorough and thoughtful review.

REFERENCES

- Ashby, M. L. N. et al. 2000, *ApJ*, 539, L115
- Aspin, C., Sandell, G., & Russell, A. P. G. 1994, *A&AS*, 106, 165
- Aspin, C. & Sandell, G. 1997, *MNRAS*, 289, 1
- Bachiller, R. 1996, *ARA&A*, 34, 111
- Bachiller, R. & Cernicharo, J. 1990, *A&A*, 239, 276
- Bally, J., Devine, D., & Reipurth, B. 1996, *ApJ*, 473, L49
- Benedettini, M., Viti, S., Giannini, T., Nisini, B., Goldsmith, P.F., & Saraceno, P. 2002, *A&A*, in press
- Bergin, E.A. & Snell, R.L. 2002, *ApJL*, submitted
- Bergin, E. A., Ciardi, D. R., Lada, C. J., Alves, J., & Lada, E. A. 2001, *ApJ*, 557, 209
- Bergin, E. A. et al. 2000, *ApJ*, 539, L129
- Bergin, E. A., Snell, R. L., & Goldsmith, P. F. 1996, *ApJ*, 460, 343
- Bergin, E. A., Melnick, G. J., Neufeld, D. A. 1998, *ApJ*, 499, 777
- Blake, G. A., Sandell, G., van Dishoeck, E. F., Groesbeck, T. D., Mundy, L. G., & Aspin, C. 1995, *ApJ*, 441, 689
- Caselli, P., Hartquist, T. W., & Havnes, O. 1997, *A&A*, 322, 296
- Ceccarelli, C. et al. 1999, *A&A*, 342, L21
- Cernicharo, J. et al. 1997, *A&A*, 323, L25
- Cernis, K. 1990, *Ap&SS*, 166, 315
- Charnley, S. B., Rodgers, S. D., & Ehrenfreund, P. 2001, *A&A*, 378, 1024.

- Codella, C., Bachiller, R., & Reipurth, B. 1999, *A&A*, 343, 585
- Di Francesco, J., Myers, P. C., Wilner, D. J., Ohashi, N., & Mardones, D. 2001, *ApJ*, 562, 770
- Fraser, H. J., Collings, M. P., McCoustra, M. R. S., & Williams, D. A. 2001, *MNRAS*, 327, 1165
- Giannini, T., Nisini, B., & Lorenzetti, D. 2001, *ApJ*, 555, 40
- Graff, M. M. & Dalgarno, A. 1987, *ApJ*, 317, 432
- Habing, H. J. 1968, *Bull. Astron. Inst. Netherlands*, 19, 421
- Harvey, P. M., Wilking, B. A., & Joy, M. 1984, *ApJ*, 278, 156
- Harwit, M., Neufeld, D. A., Melnick, G. J., & Kaufman, M. J. 1998, *ApJ*, 497, L105
- Hodapp, K. & Ladd, E. F. 1995, *ApJ*, 453, 715
- Joblin, C., Tielens, A. G. G. M., Geballe, T. R., & Wooden, D. H. 1996, *ApJ*, 460, L119
- Kaufman, M. J. & Neufeld, D. A. 1996, *ApJ*, 456, 611
- Kaufman, M. J., Wolfire, M. G., Hollenbach, D. J., & Luhman, M. L. 1999, *ApJ*, 527, 795
- Knee, L. B. G. & Sandell, G. 2000, *A&A*, 361, 671
- Lada, C. J., Alves, J., & Lada, E. A. 1996, *AJ*, 111, 1964
- Langer, W. D., Castets, A., & Lefloch, B. 1996, *ApJ*, 471, L111
- Lefloch, B., Castets, A., Cernicharo, J., & Loinard, L. 1998, *ApJ*, 504, L109
- Lefloch, B., Castets, A., Cernicharo, J., Langer, W. D., & Zylka, R. 1998, *A&A*, 334, 269
- Liseau, R. et al. 1996, *A&A*, 315, L181
- Maret S., Ceccarelli C., Caux E., Tielens A.G.G.M., Castets A., Parise B. 2002, *A&A*, submitted
- May, P. W., Pineau des Forêts, G., Flower, D. R., Field, D., Allan, N. L., & Purton, J. A. 2000, *MNRAS*, 318, 809
- Melnick, G. J. et al. 2000a, *ApJ*, 539, L87

- Melnick, G. J. et al. 2000b, ApJ, 539, L77
- Molinari, S. et al. 2000, ApJ, 538, 698
- Moneti, A., Cernicharo, J. ;, & Pardo, J. R. ;, 2001, ApJ, 549, L203
- Neau, A. et al. 2000, J. Chem. Phys., 113, 1762
- Neufeld, D. A. et al. 2000a, ApJ, 539, L107
- Neufeld, D. A. et al. 2000b, ApJ, 539, L111
- Nisini, B. et al. 1999, A&A, 350, 529
- Nisini, B., Benedettini, M., Giannini, T., Codella, C., Lorenzetti, D., Di Giorgio, A.M., & Richer, J. S. 2000, A&A, 360, 297
- Phillips, T. R., Maluendes, S., & Green, S. 1996, ApJS, 107, 467
- Reipurth, B. 1999, *A general catalog of Herbig-Haro objects*, 2. edition, <http://casa.colorado.edu/hhcat>
- Rudolph, A. L., Bachiller, R., Rieu, N. Q., Van Trung, D., Palmer, P., & Welch, W. J. 2001, ApJ, 558, 204
- Sandell, G. ;. & Knee, L. B. G. 2001, ApJ, 546, L49
- Sandell, G., Knee, L. B. G., Aspin, C., Robson, I. E., & Russell, A. P. G. 1994, A&A, 285, L1
- Schilke, P., Walmsley, C. M., Pineau Des Forets, G., & Flower, D. R. 1997, A&A, 321, 293
- Snell, R. L. et al. 2000a, ApJ, 539, L101
- Snell, R. L. et al. 2000b, ApJ, 539, L93.
- Snell, R. L. et al. 2000c, ApJ, 539, L97.
- Snell, R. L. & Edwards, S. 1981, ApJ, 251, 103
- Spaans, M. & van Dishoeck, E. F. 2001, ApJ, 548, L217.
- Tafalla, M. et al. 2002, ApJ, in press
- Tielens, A. G. G. M. & Hagen, W. 1982, A&A, 114, 245

- Tielens, A. G. G. M. & Hollenbach, D. 1985, *ApJ*, 291, 722
- Uchida, K. I., Sellgren, K., Werner, M. W., & Houdashelt, M. L. 2000, *ApJ*, 530, 817
- Viti, S., Roueff, E., Hartquist, T. W., Pineau des Forêts, G., & Williams, D. A. 2001, *A&A*, 370, 557.
- Wagner, A. F. & Graff, M. M. 1987, *ApJ*, 317, 423
- Warin, S., Castets, A., Langer, W. D., Wilson, R. W., & Pagani, L. 1996, *A&A*, 306, 935
- Wright, C. M., van Dishoeck, E. F., Black, J. H., Feuchtgruber, H., Cernicharo, J., González-Alfonso, E., & de Graauw, T. 2000, *A&A*, 358, 689
- Ziurys, L. M., Friberg, P., & Irvine, W. M. 1989, *ApJ*, 343, 201

Table 1. SWAS Survey Sample Positions

SWAS Survey No.	$\Delta\alpha(^{\circ})$	$\Delta\delta(^{\circ})$	Source ^a	Time (hrs)	rms (mK) ^b
SS1	−0.8	7.2	...	32.8	8
SS2	−1.5	5.0	SVS 12	35.6	11
SS3	−5.6	3.2	...	30.0	10
SS4	1.5	2.2	IRAS 7	61.0	7
SS5	−2.2	2.2	...	57.5	8
SS6	0.0	0.0	SVS 13	29.6	11
SS7	−1.6	−1.6	IRAS 2	29.0	12
SS8	1.5	−2.1	IRAS 4	37.3	9
SS9	−4.2	−4.3	...	26.2	10

^aOnly associations with well studied IRAS or SVS sources are noted.

^bTypical rms in 557 GHz band, system temperatures were ~ 2100 K with minimal scatter around this value.

Table 2. Observed Transitions and Telescope Parameters

Molecule	Transition	ν (GHz)	E_u (K)	Telescope	Δv_{res} (km s ^{−1})	θ_{MB}	η_{MB}	t_{int} (m)	$\sigma(T_A^*)$ (mK)
H ₂ O ^a	$J = 1_{10} \rightarrow 1_{01}$	556.93600	61.0 ^b	SWAS	1.00	3'3 × 4'5	0.90
¹³ CO ^a	$J = 5 \rightarrow 4$	550.92630	79.3	SWAS	1.00	3'3 × 4'5	0.90
¹² CO	$J = 1 \rightarrow 0$	115.27120	5.5	FCRAO	0.52	45''	0.45	6.5	200
¹³ CO	$J = 1 \rightarrow 0$	110.20137	5.3	FCRAO	0.21	48''	0.50	1.3	300
C ¹⁸ O	$J = 1 \rightarrow 0$	109.78218	5.3	FCRAO	0.43	47''	0.50	6.8	90
CH ₃ OH	$J = 2_0 \rightarrow 1_0A^+$	96.74142	7.0	FCRAO	0.48	54''	0.50	16.0	30
N ₂ H ⁺	$J = 1 \rightarrow 0$	93.17378	4.5	FCRAO	0.50	56''	0.50	4.3	70
HCO ⁺	$J = 1 \rightarrow 0$	89.18855	4.3	FCRAO	0.53	58''	0.45	11.3	50
SiO	$J = 2 \rightarrow 1$	86.84696	6.3	FCRAO	0.54	60''	0.45	18.0	30

^aIntegration time and sensitivities given in Table 1.

^bTransition is 27 K above o-H₂O ground state.

Table 3. Data, Estimated Source Properties, and Results – NGC 1333 Outflows

	IRAS 4 (1.5,-2.1)	IRAS 2 (-1.6,-1.6)	HH7-11 (0.0,0.0)	IRAS 7 (1.5,2.2)
<u>o-H₂O 1₁₀ – 1₀₁ (SWAS):</u>				
$\int T_A^* dv$ (K km/s)	1.27±0.06	1.89±0.08	1.60±0.06	0.51±0.03
Δv (km s ⁻¹)	24.4±0.8	24.7±1.3	27.8±1.5	8.5±0.8
<u>o-H₂O 2₁₂ – 1₀₁ (ISO):</u>				
$\int S_\nu d\nu$ (W cm ⁻²) ^a	2.8 × 10 ⁻¹⁹	1.6 × 10 ⁻¹⁹	1.5 × 10 ⁻¹⁹	...
<u>CO 1–0 (FCRAO-conv. 4'):</u>				
$\int T_A^* dv$ (K km/s)	8.9±0.3	14.7±0.3	21.5±0.3	8.9±0.4
Δv (km s ⁻¹)	11.4±0.3	11.1±0.2	11.7±0.1	12.0±0.5
<u>Estimated Properties and Results:</u>				
n(H ₂) (cm ⁻³)	1 × 10 ⁵	3 × 10 ⁵	5 × 10 ⁴	6 × 10 ⁴
Temperature (K)	75 ^b	40 ^c	50 ^d	40 ^e
$\int S_\nu d\nu$ (W cm ⁻²) [179 μm] ^f	3.5 × 10 ⁻²¹	2.8 × 10 ⁻²¹	2.3 × 10 ⁻²¹	1.1 × 10 ⁻²¹
N(o-H ₂ O) (cm ⁻²)	3 × 10 ¹⁴	3 × 10 ¹⁴	1 × 10 ¹⁵	6 × 10 ¹⁴
N(CO) (cm ⁻²) ^g	8 × 10 ¹⁶	7 × 10 ¹⁶	1 × 10 ¹⁷	4 × 10 ¹⁶
x(o-H ₂ O)	4 × 10 ⁻⁷	4 × 10 ⁻⁷	1 × 10 ⁻⁶	1 × 10 ⁻⁶

^aTotal fluxes from outflow derived using data obtained from the ISO data archive using ISAP version 2.0a and LWS calibration version 8.

^bEstimated by Blake et al. (1995) from CS and H₂CO.

^cAdopt value used by (Langer, Castets, & Lefloch 1996) in their analysis of multi-transitional CS data.

^dRudolph et al. (2001) estimate T = 10 – 40 K on the basis of VLA NH₃ observations, while Codella, Bachiller, & Reipurth (1999) derive 50 K from SiO observations. We adopt the latter value.

^eNo previous estimates in the literature.

^fPredicted o-H₂O 179 μm emission from single component (constant density and temperature) model that reproduces the 557 GHz emission (§4.1.2).

^gEstimated by convolving FCRAO data to 4'. To separate outflow and quiescent gas emission the convolved spectra were fit with multi-component Gaussians. Column density is derived assuming LTE at the temperature listed here.

Table 4. Data, Estimated Source Properties, and Results –
NGC 1333 Ambient Gas

	SS1 (-0.8,7.2)	SVS 12 (-1.5,5.0)	SS5 (-2.1,2.2)
<u>o-H₂O 1₁₀ – 1₀₁ (SWAS):</u>			
$\int T_A^* dv$ (K km/s)	0.19±0.02	0.24±0.03	0.19±0.02
v (km s ⁻¹)	6.4±0.2	6.9±0.2	7.3±0.2
Δv (km s ⁻¹)	3.7±0.6	3.0±0.4	2.8±0.5
<u>C¹⁸O 1–0 (FCRAO-conv. 4′):</u>			
$\int T_A^* dv$ (K km/s)	1.67±0.04	1.71±0.04	1.35±0.04
v (km s ⁻¹)	7.9±0.1	8.0±0.1	8.1±0.1
Δv (km s ⁻¹)	1.9±0.1	2.1±0.1	2.2±0.1
<u>Estimated Properties and Results:</u>			
n(H ₂) (cm ⁻³)	2 × 10 ⁴	1 × 10 ⁴	1 × 10 ⁴
Temperature (K)	20	20	20
N(o-H ₂ O) (cm ⁻²)	3 × 10 ¹⁵	3 × 10 ¹⁵	2 × 10 ¹⁵
N(C ¹⁸ O) (cm ⁻²)	4 × 10 ¹⁵	5 × 10 ¹⁵	3 × 10 ¹⁶
x(o-H ₂ O)	1 × 10 ⁻⁷	1 × 10 ⁻⁷	8 × 10 ⁻⁸

Table 5. ^{13}CO J = 5–4 Line Parameters

SWAS Survey No.	$\Delta\alpha(')$	$\Delta\delta(')$	Source	$\int T_A^* dv$ (K km s $^{-1}$)	v (km s $^{-1}$)	Δv (km s $^{-1}$)
SS1	−0.8	7.2	...	4.34±0.06	7.9±0.1	2.3±0.1
SS2	−1.5	5.0	SVS 12	4.03±0.06	8.0±0.1	2.2±0.1
SS3	−5.6	3.2	...	0.26±0.05	8.5±0.1	1.9±0.1
SS4	1.5	2.2	IRAS 7	1.89±0.06	8.5±0.1	2.2±0.1
SS5	−2.2	2.2	...	1.44±0.05	8.3±0.1	2.5±0.1
SS6	0.0	0.0	SVS 13	2.42±0.05	8.4±0.1	2.4±0.1
SS7	−1.6	−1.6	IRAS 2	1.86±0.05	8.1±0.1	2.4±0.1
SS8	1.5	−2.1	IRAS 4	1.10±0.05	8.0±0.1	2.6±0.1
SS9	−4.2	−4.3	...	0.28±0.06	7.8±0.1	3.1±0.1

Table 6. PDR Model Results for NGC1333

Position	G_0	$\langle x(\text{H}_2\text{O}) \rangle$	$x(\text{H}_2\text{O})_{max}$	^{13}CO J = 5–4 (K km/s)		$\text{o-H}_2\text{O}$ $1_{10} - 1_{01}$ (K km/s)	
				Model	Obs.	Model	Obs.
SS1	400	2.0×10^{-7}	4×10^{-7}	2.25	4.34±0.06	0.25	0.19±0.02
SS2(SVS12)	400	2.0×10^{-7}	4×10^{-7}	2.25	4.03±0.06	0.25	0.24±0.02
SS5	100	1.8×10^{-7}	4×10^{-7}	1.35	1.44±0.05	0.17	0.19±0.02
	1	3.6×10^{-7}	4×10^{-7}	0.01	...	0.03	...

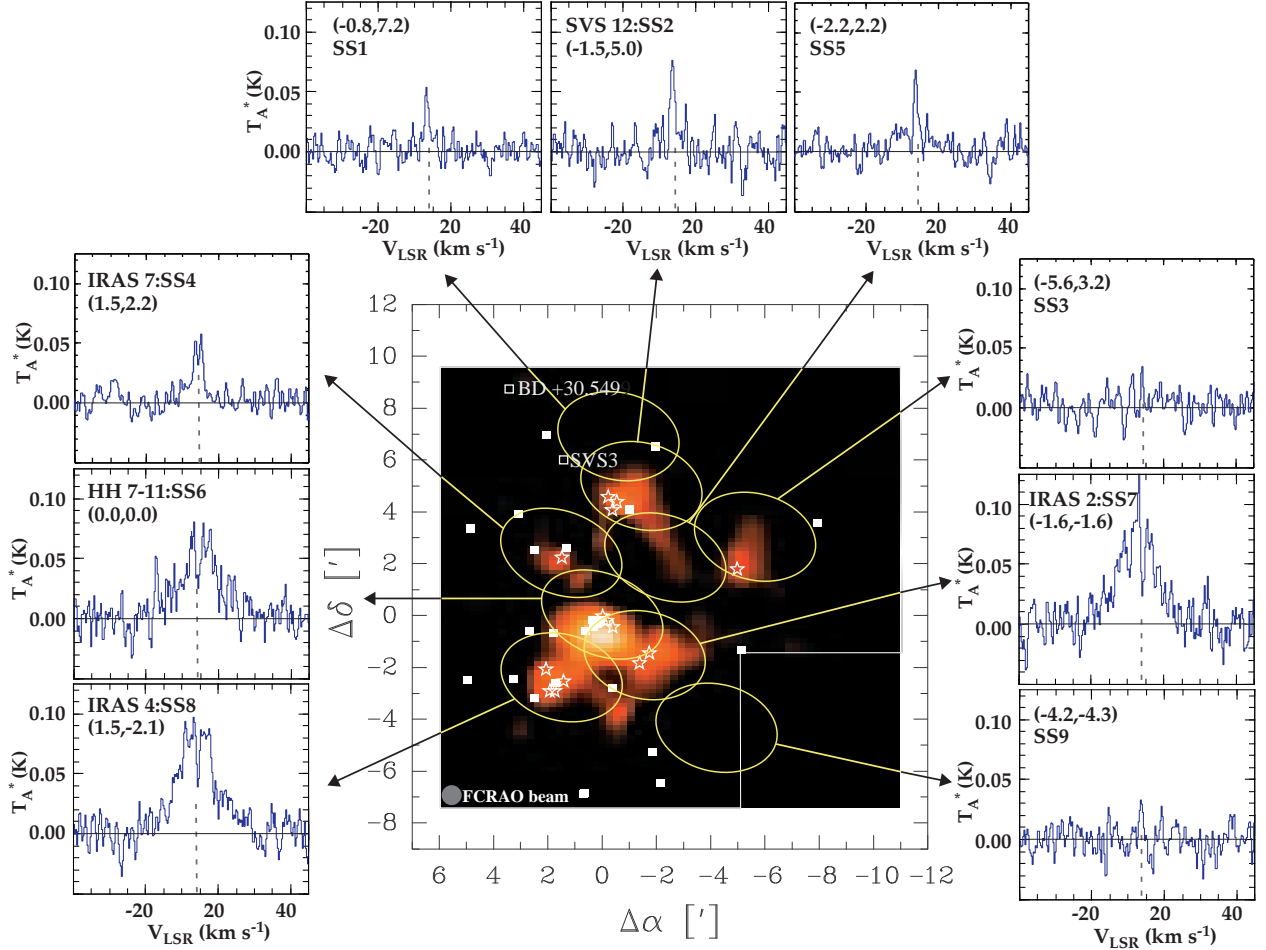


Fig. 1.— Spectra of the $1_{10}-1_{01}$ 556.936 GHz transition of ortho-water vapor from the various positions in NGC 1333. Each spectra is labeled with any prominent source that is centered or within the beam, along with the SWAS survey position number (Table 1). Placements of the elliptical SWAS beam at the observed rotation angle are shown superposed on a map of integrated N_2H^+ ($J=1-0$) emission. The scale of the N_2H^+ emission ranges from 1 K $km\ s^{-1}$ to 8 K $km\ s^{-1}$ and is integrated over all hyperfine components. The dashed line in each spectra is the velocity of the ambient gas as determined by Gaussian fits to the N_2H^+ spectra (convolved to a circularized $4'$ SWAS beam). The stars show the location of IRAS sources and SVS 13 (0.0,0.0), while the solid squares are positions of known HH objects (see text for references). The open squares denote the positions of two stars associated with reflection nebulosity, BD +30.549 and SVS 3. Labels for other well known sources are provided in Figure 4. The map is reference to the position of SVS 13.

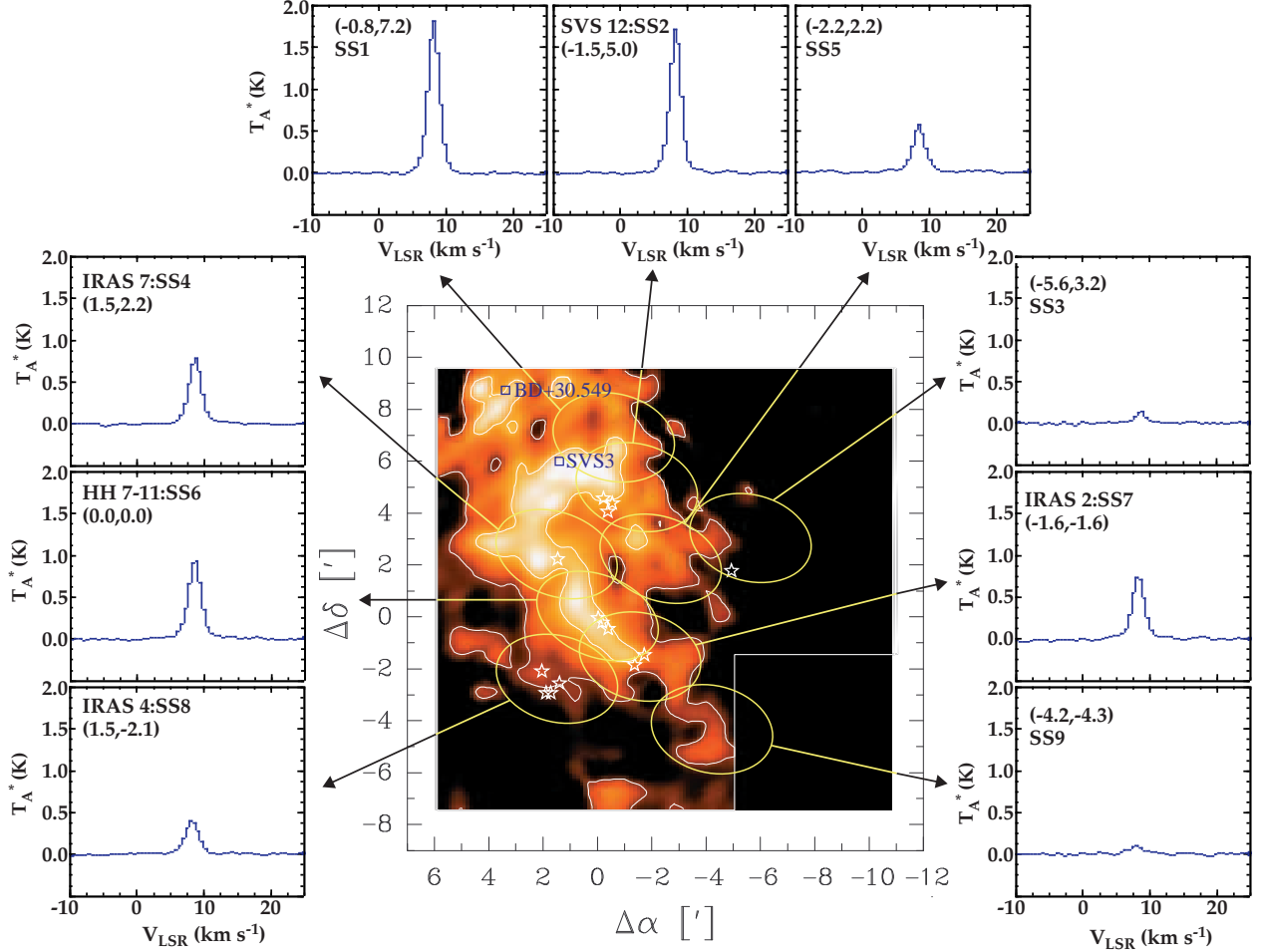


Fig. 2.— Spectra of the $J = 5-4$ transition of ^{13}CO from the various positions in NGC 1333. Each spectra is labeled with any prominent source that is centered or within the beam, along with the SWAS survey position number (Table 1). Placements of the elliptical SWAS beam at the observed rotation angle are shown superposed on a map of integrated ^{13}CO ($J=1-0$) emission. The scale of the ^{13}CO ($J=1-0$) emission ranges from 8 K km s^{-1} to 22 K km s^{-1} and is clipped to emphasize the strongest regions of emission. The stars show the location of IRAS sources and SVS 13 (0.0,0.0). The open squares denote the positions of two stars associated with reflection nebulosity, BD +30.549 and SVS 3. Labels for other well known sources are provided in Figure 4. The map is reference to the position of SVS 13.

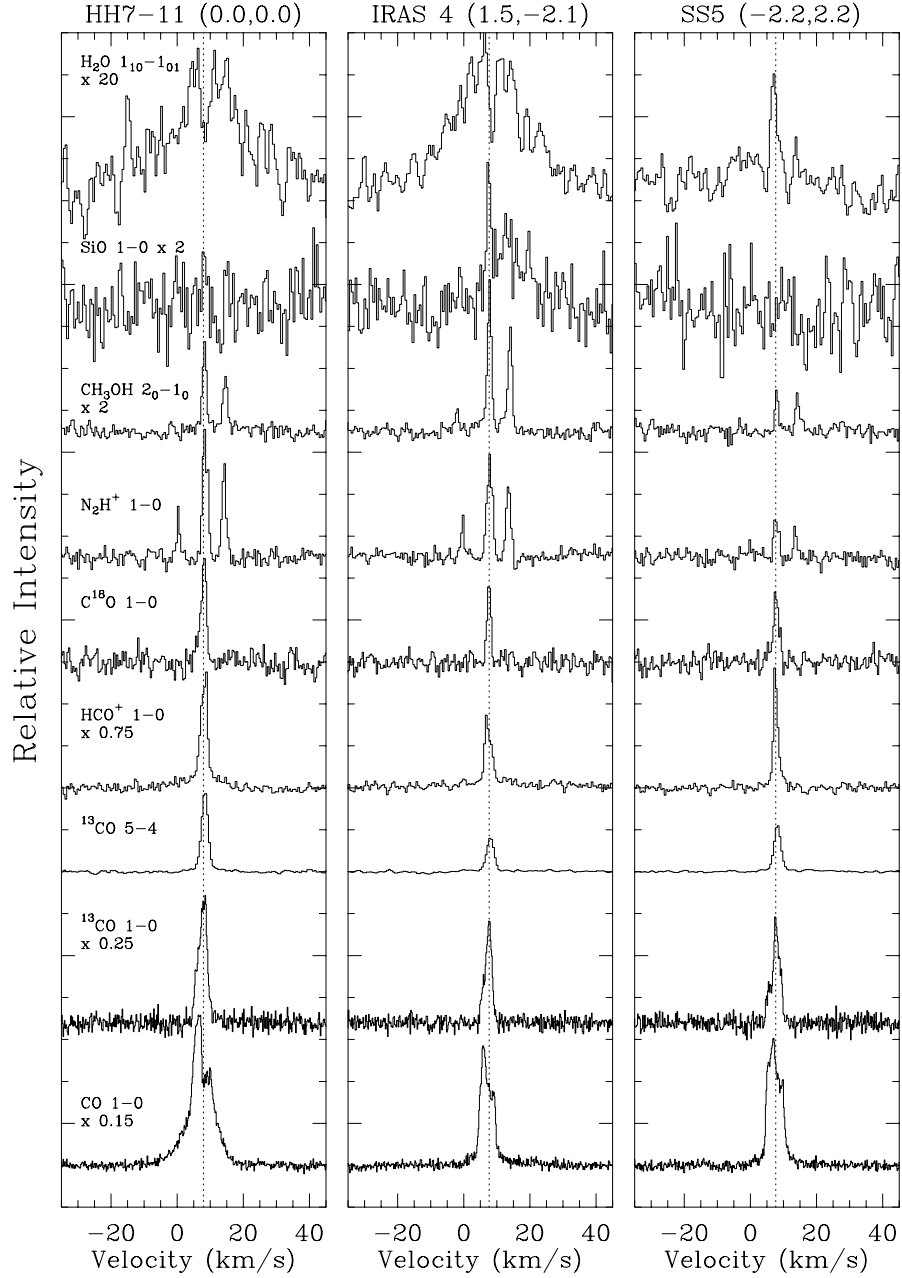


Fig. 3.— Representative spectra of each molecule and transition in this study towards positions coincident with SVS 13 (HH7-11), IRAS 4, and SS5. The spectra are given at the observed resolution (see Table 2). The y-axis is relative intensity, but for scale towards SVS 13 the HCO^+ $J=1-0$ peak intensity is $T_A^* = 1.83$ K, IRAS 4 $T_A^* = 1.14$ K, SS5 $T_A^* = 1.35$ K. The vertical line is the cloud velocity determined via Gaussian fits to the N_2H^+ emission.

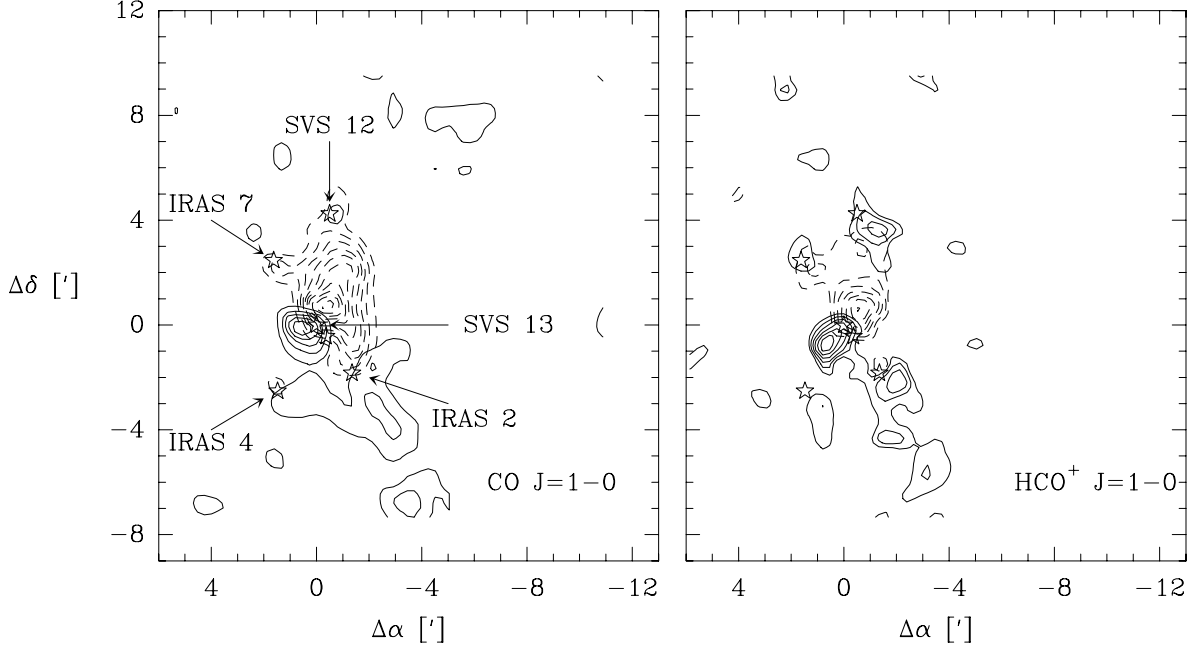


Fig. 4.— Left: Distribution of high velocity CO ($J=1-0$) emission in NGC 1333. Blue-shifted ($-20 - 4$ km s $^{-1}$) is shown as solid contours and red-shifted ($11 - 30$ km s $^{-1}$) as dashed contours. Levels begin at 3 K km s $^{-1}$ (3σ) and step at 3 K km s $^{-1}$. Locations and names of various well known sources are provided. Right: Distribution of high velocity HCO $^+$ ($J=1-0$) emission. Blue-shifted ($-8 - 5$ km s $^{-1}$) is given as solid contours and red-shifted ($11 - 20$ km s $^{-1}$) as dashed contours. Levels start at 0.6 K km s $^{-1}$ (3σ) and step at 0.2 K km s $^{-1}$. The maps are referenced to the position of SVS 13.

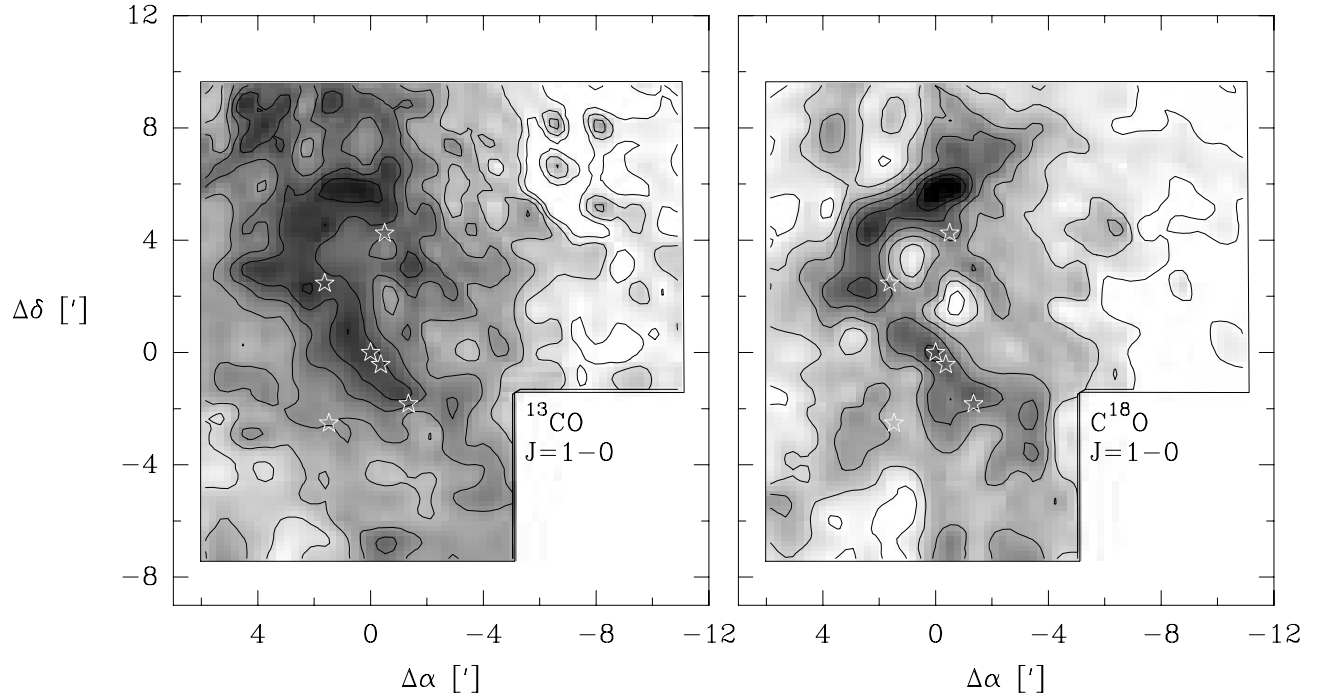


Fig. 5.— Integrated emission maps of ^{13}CO J=1-0 (left) and C^{18}O J=1-0 (right). For both panels the levels begin and step at the 3σ value, 3.0 K km s^{-1} for ^{13}CO and 0.5 K km s^{-1} for C^{18}O . The maps are referenced to the position of SVS 13.

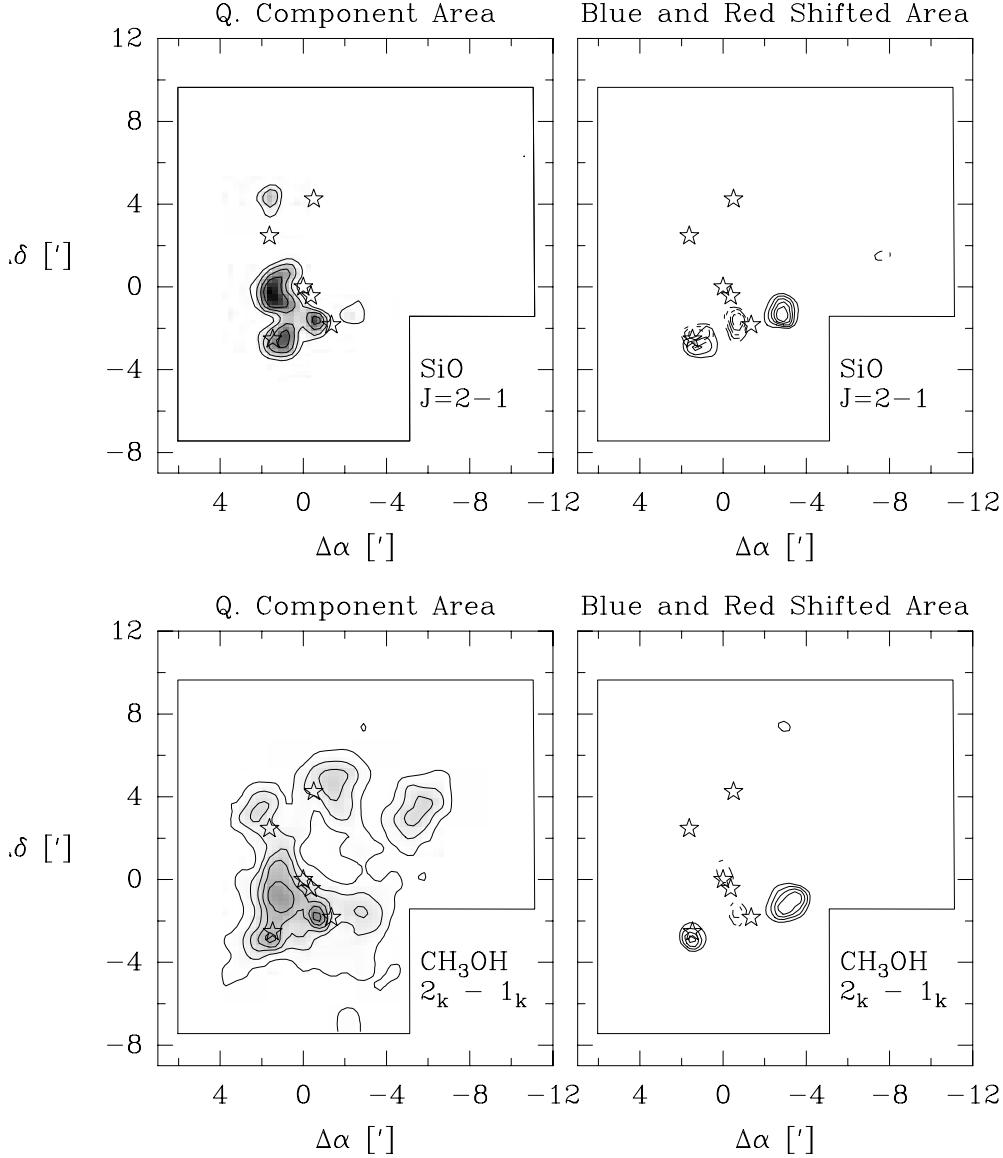


Fig. 6.— Top Panels [Left]: Integrated emission map of thermal SiO $J=2-1$ in the ambient ($6.3 - 9.5 \text{ km s}^{-1}$) gas. Contour levels begin at the 3σ level of 0.15 K km s^{-1} and step at 0.1 K km s^{-1} . [Right]: Distribution of high velocity SiO $J=2-1$ emission. Blue-shifted ($-7 - 6 \text{ km s}^{-1}$) emission is given as solid contours and red-shifted ($9 - 26 \text{ km s}^{-1}$) as dashed. For both blue- and red-shifted emission the contours begin at the 3σ level of 0.3 K km s^{-1} and step at 0.2 K km s^{-1} . Bottom Panels [Left]: Integrated emission of $\text{CH}_3\text{OH } J_k = 2_k - 1_k$ ($k = 0\text{-E}, 0\text{-A}^+, \text{ and } -1\text{-E}$) in the ambient ($-2.6 - 0.6, 6.3 - 10.0, 12.6 - 16.0 \text{ km s}^{-1}$) gas. Contour levels begin and step at the 3σ level of 0.3 K km s^{-1} . [Right]: Distribution of high velocity $\text{CH}_3\text{OH } J_k = 2_k - 1_k$ emission. Blue-shifted ($-9 - 6 \text{ km s}^{-1}$) emission is given as solid contours and red-shifted ($16 - 32 \text{ km s}^{-1}$) as dashed contours. The velocity range is chosen to avoid confusion with the strongest k components. The blue-shifted emission contains minimal contamination from the $2_0 - 1_0\text{E}$ component in the ambient gas. Contour levels for both begin at the 3σ level of 0.2 K km s^{-1} and step at 0.3 K km s^{-1} . All maps are referenced to the position of SVS 13.

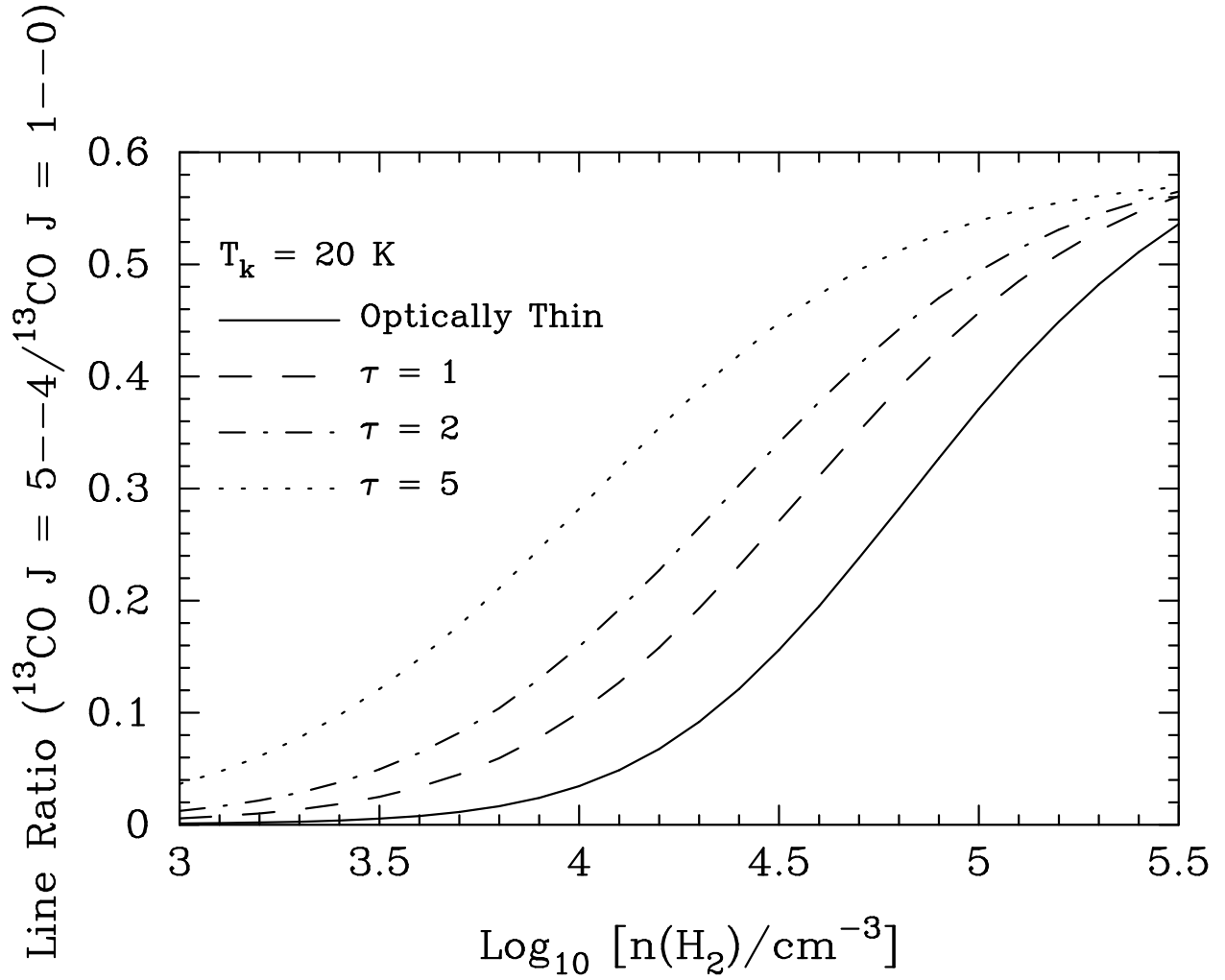


Fig. 7.— $^{13}\text{CO } J=5-4/J=1-0$ line intensity ratio from a large velocity gradient excitation model plotted as a function of density and $^{13}\text{CO } J = 1-0$ opacity (column density) for $T = 20 \text{ K}$.

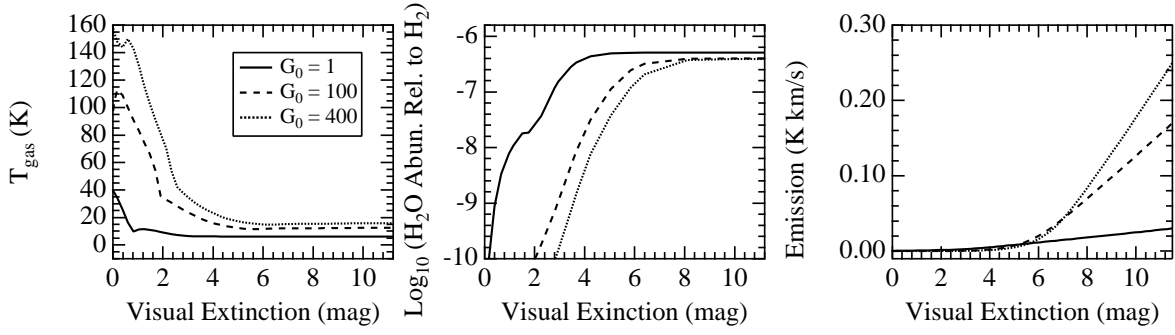


Fig. 8.— [Left:] Gas temperature as a function of cloud depth (visual extinction) for three different PDR models. [Middle:] Water abundance relative to H_2 as a function of cloud depth for same models. [Right:] Plot of integrated emission in K km/s as a function of visual extinction.